



Effect of the synthesis conditions of Ni/Al₂O₃ catalysts on the biogas decomposition to produce H₂-rich gas and carbon nanofibers



S. de Llobet, J.L. Pinilla, R. Moliner, I. Suelves*

Instituto de Carboquímica, CSIC, C/Miguel Luesma 4, 50018 Zaragoza, Spain

ARTICLE INFO

Article history:

Received 16 July 2014

Received in revised form

30 September 2014

Accepted 3 October 2014

Available online 12 October 2014

Keywords:

Biogas

Catalytic decomposition

H₂-rich gases

Ni-catalysts

Carbon nanofibers

ABSTRACT

The utilization of biogas as carbon source for the co-production of filamentous-like materials and syngas is proposed. Catalysts with different Ni:Al molar ratios, Al₂O₃ supports and preparation methods were synthesized. The suitability of the catalysts was analyzed considering activity, stability and carbon yield. Catalysts showed a good performance and similar results according to syngas compositions were obtained. However, some differences related to stability over time and carbon yields were detected. TPR analysis and TEM micrographs of the fresh catalysts revealed the presence of two different Ni particles: large Ni particles with low metal support interaction (MSI) that favoured the formation of encapsulating carbon and small Ni particles inserted in the Al₂O₃ structure with a greater MSI that lead to nanofilamentous carbons formation. Generally both kinds of Ni particles were observed in all catalysts, however their relative abundance was dramatically affected by the Al₂O₃ employed, the preparation method and the Ni:Al molar ratio.

© 2014 Elsevier B.V. All rights reserved.

1. Introduction

Biogas is generated from the anaerobic digestion of the organic matter (agricultural wastes, landfills and urban and industrial wastewaters). Commonly, biogas is released into the atmosphere or directly burned in an internal combustion engine [1]. Most recently, different alternatives for biogas utilisation have been proposed such as bio-methane production [2], combustion in a dual fuel diesel engine [3,4] or as feedstock in the dry reforming of CH₄ (DRM) [5,6]. In the latter case, high CO₂ concentration, up to 50%, makes biogas a perfect choice to be used as feedstock, resulting in a suitable syngas that can be used for hydrogen production [7,8], to feed a solid oxide fuel cell [9] or for hydrocarbons synthesis via the Fischer–Tropsch process [10]. Besides this, DRM using biogas can be classified as environmentally friendly due to the renewable character of the feedstock. However, the utilization of biogas in the DRM faces many challenges, being the energy required to carry out the process (CH₄ + CO₂ → 2H₂ + 2CO, ΔH° = 247 kJ mol^{−1}), catalyst poisoning caused by biogas minor compounds [11–13] and catalyst deactivation by carbon deposition [14] among the most important.

Catalyst deactivation is commonly associated to carbon deposition, and efforts in DRM are focused on the synthesis of catalysts

with low amounts of active metals in order to generate small crystallites that inhibit carbon formation [15]. However, only encapsulating carbon is responsible of catalyst deactivation [16,17]. During DRM, other carbon structures can be obtained [18,19], being the nanofilamentous carbons (NCs) of special interest. Even though NCs are not directly responsible of catalyst deactivation, they can cause reactor plugging [20]. This situation can be solved by using a fluidized bed reactor instead of a fixed bed reactor [21]. NCs are high valuable materials [22] that depending on their structure and surface properties can be employed in different applications [23,24]. The condition of the DRM using biogas as feedstock can be adjusted so that the formation of NCs without catalyst deactivation can be achieved. Therefore, biogas is used as carbon source for the co-production of filamentous-like materials and a H₂ rich gas with very interesting combustion properties [25]. This biogas valorization route has been previously studied by our group [25–27] and it is known as catalytic decomposition of biogas (CDB). Conceptually, this process is similar to the catalytic decomposition of methane (CDM) [21,28–30]. Metals belonging to groups 8–10 (Ni, Co and Fe) and supported on different metal oxides (Al₂O₃, SiO₂ or MgO) have been traditionally used in the CDM to generate NCs [31]. From the carbon yield point of view, catalyst metal content plays an important role. High metal loading catalysts are favorable for hydrogen and NCs production [30]. Ermakova et al. [32] and Li et al. [33] observed that carbon yield was proportional to the Ni concentration in the catalyst. However, Takenaka et al. [34]

* Corresponding author. Tel.: +34 976 73 3977; fax: +34 976 73 3318.
E-mail address: isuelves@icb.csic.es (I. Suelves).

reported a great carbon yield ($491 \text{ gC g}_{\text{Ni}}^{-1}$) with a 40% Ni/SiO₂ catalyst. Support also plays an important role. Unsupported Ni catalysts barely generate NCs when CH₄ is decomposed [33,35], while a production up to $385 \text{ gC g}_{\text{Ni}}^{-1}$ was reported when using a 90% Ni/SiO₂ catalyst [32]. Many studies have also related NCs growth with Ni crystal domain size. Chen et al. [36] observed an optimal Ni crystal size of 34 nm while Pinilla et al. [37] obtained the best results with catalysts with a Ni crystal domain size after reaction between 10 and 20 nm. Little information considering NCs production from biogas has been published. Besides previous works carried out by our research group [26,27,38], for the best of our knowledge, only Corthals et al. [39] considered biogas as an interesting source for NCs generation. Carbon yields up to 37.2 and $19.1 \text{ gC g}_{\text{Ni}}^{-1}$ were achieved with a Ni(30)SrTiO₃ catalyst when decomposing biogas at 600 °C with a CH₄:CO₂ ratio of 2 and 1, respectively.

The purpose of this work is to synthesize different Ni/Al₂O₃ catalysts to study how their properties can affect its performance in the CDB. Thus, two different Ni:Al molar ratios (30:70 and 67:33), two different Al₂O₃ and two different preparation methods (impregnation and fusion) were used to prepare catalysts with different characteristics. The suitability of the catalysts was analyzed considering activity, stability and carbon yield. Additionally, the NCs produced were characterised by different techniques (XRD, N₂ adsorption, TEM) in order to address the effect of the different catalysts characteristics on the NCs properties and morphology.

2. Experimental

2.1. Aluminas synthesis

Two aluminas with different surface properties were used as support. An organized mesoporous alumina (OMA-Al₂O₃) was synthesized according to a procedure available in [40]. Briefly, aluminium isopropoxide was dissolved in ethanol and propanol with 1, 8 and 6 molar ratios, respectively. Then, a non-ionic surfactant (Pluronic F127) was added in a 0.01 molar ratio to the mixture with constant stirring at 50 °C. When the surfactant was dissolved, water was added in an 11 molar ratio to create an emulsion. All molar ratios are expressed in reference to aluminium isopropoxide. The surfactant and solvents were later removed by subsequent drying steps at 150 and 350 °C and through calcination at 600 °C for 4 h. The second alumina (SIG-Al₂O₃), was directly obtained after the calcination of Sigma-Aldrich aluminium nitrate (Al(NO₃)₃·9H₂O) at 450 °C for 8 h.

2.2. Catalysts synthesis

Four different catalysts were synthesized, two with a Ni:Al molar ratio of 67:33 and two with a Ni:Al molar ratio of 30:70. Catalysts with a high Ni content (67 mol.%) were prepared by the fusion method previously described in [41]. Summarizing, nickel nitrate (Ni(NO₃)₂·6H₂O) was mixed and crushed with one of the aforementioned aluminas (OMA-Al₂O₃ or SIG-Al₂O₃), followed by calcination of the resulting mixture at 450 °C for 8 h. Catalysts with a low Ni content (30 mol.%) were prepared by the incipient wetness impregnation method with impregnation of an aqueous solution of the nickel nitrate (Ni(NO₃)₂·6H₂O). The resultant slurry was dried at 110 °C during night and calcined in air flow at 450 °C for 8 h. In all cases, the powder samples obtained after calcination were ground and sieved to allow the selection of 100–200 μm particle size.

Calcined catalysts were named as NiO-X-Y, where “X” refers to the Ni molar content (30 or 67) and “Y” to the alumina employed (OMA or SIG). Therefore, NiO-30-OMA stands for a catalyst with a Ni:Al molar content of 30:70 and prepared with the OMA-Al₂O₃.

Table 1
Synthesis parameters of the prepared catalysts.

Name	Ni:Al molar ratio	Al ₂ O ₃	Method
NiO-30-OMA	30:70	OMA	Impregnation
NiO-30-SIG	30:70	SIG	Impregnation
NiO-67-OMA	67:33	OMA	Fusion ^a
NiO-67-SIG	67:33	SIG	Fusion ^a
NiO-67-SIG2	67:33	SIG	Fusion ^b

^a Prepared by mixing Ni nitrate with the previously calcined Al₂O₃.

^b Prepared by mixing at the same time Ni and Al nitrates.

Reduced catalysts are named in the same way but substituting “NiO” by “Ni”.

Results obtained with the NiO-67-SIG catalyst were very poor as compared with the other catalysts, especially in terms of carbon yield. For that reason, a fifth catalyst with a Ni:Al molar ratio of 67:33 and named NiO-67-SIG2 was synthesized. The preparation method was similar to that employed to prepare the NiO-67-SIG catalyst but in this case both nitric salts of Ni and Al were crushed and mixed together, followed by calcination of the mixture at 450 °C for 8 h. A summary report of the different catalysts synthesized is shown in Table 1.

2.3. Experimental procedure

To carry out the experiments, a synthetic CH₄:CO₂ mixture with a volume ratio of 60:40 was used. This volume ratio was chosen in order to mimic biogas composition. Catalytic experiments were carried out in a fixed-bed quartz reactor, 15 mm i.d, 750 mm height, fed by the top and heated by an electric furnace. A Peltier cooler was placed after the reactor to condense steam formed during the reaction. Tests were performed at a reaction temperature of 700 °C and 0.05 g of catalyst were loaded in the reactor. Before each test, catalysts were in-situ reduced with an H₂ flow of 100 mL min^{−1} at 550 °C for 1 h. Then, a synthetic biogas flow rate of 100 mL min^{−1} was fed into the reactor for 3 h. The weight hourly space velocity (WHSV, defined here as the total flow rate at normal conditions per gram of catalyst initially loaded) was 120 L_N g_{cat}^{−1} h^{−1}.

In order to determine the outlet gases composition (syngas composition), bag samples were taken and analysed by means of gas chromatography in a micro GC Varian CP4900 equipped with two packed columns (Molecular Sieve and Porapak) and a TCD detector to quantify H₂, CO, CH₄ and CO₂ concentrations.

CH₄ conversions, $X_{\text{CH}_4,t}$ (Eq. 1), reaction rates, $(-r_{\text{CH}_4,t})$ (Eq. 2) and sustainability factors, $S.F._{\text{CH}_4}$ (Eq. 3) were calculated as follows:

$$X_{\text{CH}_4,t} = \frac{(F_{\text{in,CH}_4,t} - F_{\text{out,CH}_4,t})}{F_{\text{in,CH}_4,t}} \times 100 \quad (1)$$

$$(-r_{\text{CH}_4,t}) = \frac{X_{\text{CH}_4,t}}{W/F_{\text{in,CH}_4,t}} \quad (2)$$

$$S.F._{\text{CH}_4} = \frac{(-r_{\text{CH}_4,180 \text{ min}})}{(-r_{\text{CH}_4,5 \text{ min}})} \quad (3)$$

In Eq. (1), $F_{\text{in,CH}_4,t}$ and $F_{\text{out,CH}_4,t}$ represent CH₄ molar flow rates entering (in) or leaving (out) the reactor at a certain reaction time (t). In Eq. (2), W represents the grams of catalyst or the grams of Ni, depending on the basis of calculation used, initially loaded in the reactor. In Eq. (3), $-r_{\text{CH}_4,180 \text{ min}}$ and $-r_{\text{CH}_4,5 \text{ min}}$ represent CH₄ reaction rates after 180 and 5 min time on stream (TOS), respectively. CH₄ sustainability factor ($S.F._{\text{CH}_4}$) was used to compare the stability of the different catalysts over time. If catalyst activity is maintained, the value of the $S.F._{\text{CH}_4}$ will be one. On the other hand, if the catalyst is completely deactivated after 180 min TOS, this value will be zero.

Table 2

Textural properties (specific surface area, pore volume and average pore diameter) and crystal domain size of the supports and calcined and reduced catalysts determined by N₂ adsorption and XRD.

	Sample	S_{BET} (m ² g ⁻¹)	V_p (cm ³ g ⁻¹)	APD (nm)	Crystal domain size (nm)
Aluminas	OMA-Al ₂ O ₃	340	1.501	15.5	–
	SIG-Al ₂ O ₃	117	0.125	4.8	–
Calcined catalysts	NiO-30-OMA	178	0.227	5.6	9.8
	NiO-30-SIG	108	0.126	7.4	25.7
	NiO-67-OMA	92	0.172	8.1	15.3
	NiO-67-SIG	47	0.074	9.7	25.4
	NiO-67-SIG2	113	0.145	5.7	9.1
Reduced catalysts	Ni-30-OMA	161	0.246	6.0	4.0
	Ni-30-SIG	102	0.129	6.4	32.6
	Ni-67-OMA	89	0.201	8.8	20.4
	Ni-67-SIG	43	0.057	6.2	58.0
	Ni-67-SIG2	98	0.162	6.6	10.9

2.4. Characterization techniques

The textural properties were measured by N₂ adsorption at 77 K in a Micromeritics Tristar apparatus. The specific surface areas and pore volumes were calculated by applying the BET method to the respective N₂ adsorption isotherms and the average pore diameter (APD) and the pore size distribution (PSD) were calculated with the BJH method based on the desorption branch of the N₂ isotherm.

XRD patterns of the calcined, reduced and spent catalysts were acquired in a Bruker D8 Advance Series 2 diffractometer equipped with a Cu (λ : 0.154 nm) anode and a secondary graphite monochromator, using a θ – θ configuration. The angle range scanned was 20–80°, using a counting step of 0.05° and a counting time per step of 3 s. The powder XRD patterns were further processed using the accompanying DIFRAC PLUS EVA 8.0 and TOPAS software.

The reducibility of the calcined catalysts was studied by temperature programmed reduction (TPR) analysis. The respective reduction profiles were obtained in an AutoChem Analyzer II 2920 (Micromeritics) provided with a TCD from a sample amount of 10 mg and using a heat rate of 5 °C min⁻¹ within a temperature range from room temperature to 1050 °C and under a flow rate of 50 mL min⁻¹ of a H₂ (10%)/Ar mixture.

The morphology of the reduced and spent catalysts was studied by transmission electron microscopy (TEM) in a JEOL-2000 FXII microscope operating at 200 keV. Standard TEM copper grids covered by a lacey amorphous carbon film were used as sample holders. The TEM was coupled to an INCA 200-X SIGHT EDX analyser operating between 136 eV and 5.9 keV.

The carbon yield (Y_c), expressed as grams of carbon generated per gram of catalyst ($g_{\text{carbon}} g_{\text{cat}}^{-1}$) or per gram of nickel ($g_{\text{carbon}} g_{\text{Ni}}^{-1}$), was determined in a Setaram Thermogravimetric Analyzer. Samples obtained after reaction were heated under air flow at a rate of 10 °C min⁻¹ from room temperature to 1000 °C. Ni oxidation was taken into account for calculations.

3. Results and discussion

3.1. Catalysts characterization

Textural properties (surface area (S_{BET}), pore volume (V_p) and average pore diameter (APD)) of the aluminas supports (OMA-Al₂O₃ and SIG-Al₂O₃) and the calcined and reduced catalysts are reported in Table 2. N₂ adsorption/desorption isotherms and pore size distributions (PSD) are included in the supporting data (Fig. S1–S6). All samples presented a type IV isotherm according to the IUPAC classification which is characteristic of mesoporous materials. Well differentiated textural properties were observed between the two aluminas synthesized. OMA-Al₂O₃ presented a surface area of 340 m² g⁻¹, a wide PSD centred at around 15.5 nm and a pore

volume of 1.501 cm³ g⁻¹. The SIG-Al₂O₃ presented worse textural properties as compared with the OMA-Al₂O₃. The surface area was three times lower (117 m² g⁻¹), the PSD was narrower and centred at 4.8 nm and the pore volume was 0.125 cm³ g⁻¹. Regarding calcined catalysts, S_{BET} , V_p and APD of the NiO-30-OMA were lower as compared with the original alumina (OMA-Al₂O₃). The impregnation with the nickel nitrate solution resulted in partial covering of the pores. Surface area and pore volume decreased to 50% and 85%, respectively. In contrast, textural properties of the NiO-30-SIG catalyst remained almost invariable after the impregnation process as compared with those of the original SIG-Al₂O₃. Surface area and pore volume were 108 m² g⁻¹ and 0.126 cm³ g⁻¹, respectively. It is noteworthy that even though NiO-30-OMA catalyst experimented a strong decrease of both surface area and pore volume, its values (178 m² g⁻¹ and 0.227 cm³ g⁻¹) were still higher than the ones obtained with the other catalysts (Table 2). Comparison between catalysts with a high Ni content, NiO-67-OMA, NiO-67-SIG and NiO-67-SIG2, and their respective aluminas is not straightforward due to the high metal loading (Ni:Al molar ratio of 67:33). In those catalysts, the alumina did not act as a support but as a textural promoter with the purpose of avoiding the coalescence of metal particles [32]. The surface area of the NiO-67-SIG (47 m² g⁻¹) was considerably lower than those of the NiO-67-OMA (92 m² g⁻¹) and the NiO-67-SIG2 (113 m² g⁻¹). The same trend was observed in terms of pore volume. NiO-67-SIG presented a pore volume of 0.074 cm³ g⁻¹, much lower than those of the Ni-67-OMA and Ni-67-SIG2 catalysts, 0.172 cm³ g⁻¹ and 0.145 cm³ g⁻¹, respectively. After the reduction treatment, textural properties of the different catalysts did not change significantly (Table 2). Surface areas were slightly reduced while pore volumes presented a little increase except for the Ni-67-SIG catalyst.

The XRD patterns of the two aluminas used to synthesize the catalysts are included in the supporting information (Fig. S7). Both aluminas showed amorphous characteristics and only the diffractogram of the OMA-Al₂O₃ revealed weak reflections corresponding to γ -Al₂O₃. The XRD patterns of the calcined catalysts are shown in Fig. 1a. Calcined catalyst presented average NiO crystal sizes ranging from 9.1 nm to 25.5 nm (Table 2). NiO-30-OMA and NiO-67-SIG2 presented the smallest average NiO crystal domain sizes, 9.8 nm and 9.1 nm, respectively. In turn, NiO-30-SIG and NiO-67-SIG showed the biggest sizes (ca. 25.5 nm). Finally, NiO-67-OMA catalyst presented an intermediate size, 15.3 nm. XRD patterns of the catalysts reduced at 550 °C are shown in Fig. 1b. In all cases, no NiO reflections were detected suggesting a complete reduction of the catalysts. Average Ni crystal sizes of reduced Ni-30-SIG, Ni-67-OMA and especially Ni-67-SIG catalysts increased as compared with the calcined ones (32.6 nm, 20.4 nm and 58.0 nm). The opposite behaviour was observed for the Ni-30-OMA catalyst (4.0 nm) while for the Ni-67-SIG2 catalyst Ni crystal size remained almost

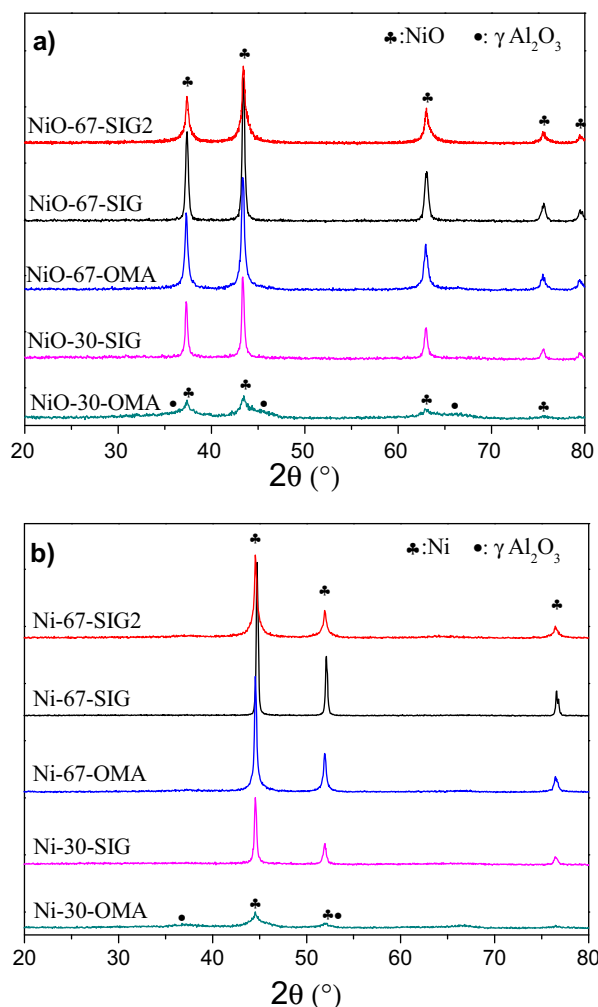


Fig. 1. Powder XRD patterns of the calcined (a) and reduced at 550 °C catalysts (b).

invariable (10.9 nm). XRD patterns of both calcined and reduced catalysts did not reveal the formation of NiAl₂O₄ species.

TEM micrographs of the reduced catalysts are shown in Fig. 2. In Ni-30-OMA micrographs (Fig. 2a) two different kinds of Ni particles were observed: small Ni particles (5–10 nm diameter) inserted in the Al₂O₃ structure and some aggregates of coarse particles around 50–100 nm (inset of Fig. 2a). It was noticed that the small Ni particles were much more abundant than the coarse ones. The high surface area of the OMA-Al₂O₃ helped obtaining a better nickel dispersion. In contrast, in the Ni-30-SIG case (Fig. 2b), the low S_{BET} and V_p of the SIG-Al₂O₃ provoked that Ni was not properly dispersed even though an impregnation method was used. As a result, Ni particles presented a great heterogeneity of sizes ranging from 20 nm to 100 nm. Nevertheless, few small Ni particles (10 nm) supported on the SIG-Al₂O₃ were also observed (inset of Fig. 2b). Micrographs took from the Ni-67-OMA and Ni-67-SIG2 catalysts (Fig. 2c and d, respectively), were similar to each other. Both samples presented big Ni particles ranging from 50 nm to 200 nm. The high Ni:Al ratio (67:33 mol.%) was the responsible of this situation. Small Ni particles supported on the Al₂O₃ structure, similar to those observed in the Ni-30-OMA catalyst, were also identified (Fig. 2c and inset of d). Its proportion was lower as compared to the Ni-30-OMA catalyst but greater than that observed in the Ni-30-SIG catalyst. TEM micrographs of the Ni-67-SIG catalyst were not taken because of the bad performance of this catalyst during the CDB as commented afterwards.

TPR profiles of calcined catalysts are included in Fig. 3. This technique is employed to identify the different Ni species and to study metal-support interactions (MSI). TPR profiles of the high Ni content catalysts, NiO-67-OMA, NiO-67-SIG and NiO-67-SIG2, were shown in Fig. 3a along with the profile of pure NiO (NiO-100). All catalysts presented a peak at ca. 350 °C, however the size of the peaks varied. NiO-67-SIG presented the biggest peak followed by the NiO-67-OMA and NiO-67-SIG2 catalysts. This peak is associated to large NiO particles that do not form significant chemical bonds with the Al₂O₃ support [42]. Besides, the reduction peak of pure NiO appeared at a similar temperature. At higher temperatures (400 °C onwards), NiO-67-SIG profile was similar to that of pure NiO and the amount of consumed H₂ was negligible. In contrast, two different peaks, with maximums at 450 °C and 610 °C approximately, were identified in the TPR profiles of the NiO-67-OMA and NiO-67-SIG2 catalysts, being slightly larger for the NiO-67-SIG2 catalyst. Wu and Hercules [43] reported two forms of nickel ions on the surface of the Al₂O₃ support: NiO ions in octahedral sites and NiO ions in tetrahedral sites of the Al₂O₃, being the former easily reduced than the latter. These two different Ni ions may correspond to the different peaks observed. The absence of NiAl₂O₄ species, confirmed by XRD, is further evidenced by the almost negligible H₂ consumption at temperatures above 720 °C [42,44,45]. Well differentiated TPR profiles were obtained for the catalysts synthesized with a low Ni content (Fig. 3b). For both catalysts, a peak located at ca. 350 °C and assigned to bulk NiO phase was observed. The second peak, positioned at higher temperatures (600–650 °C), is ascribed to difficult to reduce NiO species [45,46]. The width of the peak (400–750 °C) suggests the contribution of different Ni species: the aforementioned NiO ions in octahedral sites and NiO ions in tetrahedral sites of the Al₂O₃. The size of the peak observed at ca. 350 °C was smaller for the NiO-30-OMA catalyst than for the NiO-30-SIG one. At higher temperatures, the situation was the opposite. The two different temperature ranges (low and high) detected for Ni reduction may be related to the different Ni particles observed in the TEM micrographs (Fig. 2). The reduction peak observed at low temperatures (350 °C) corresponds to big Ni particles since this kind of particles were predominantly observed in the Ni-30-SIG catalyst. In turn, small Ni particles inserted in the Al₂O₃ structure, mainly observed in the Ni-30-OMA catalyst, can be associated to the wide peak detected at higher temperatures.

Same metal content, calcination temperature or preparation methods were used to synthesized NiO-30-OMA and NiO-30-SIG catalysts. Therefore, differences observed in the textural properties (N₂ adsorption), Ni crystal domain sizes (XRD), MSI (TPR) and proportion between small Ni particles inserted in the Al₂O₃ structure and big Ni particles (TEM) are due to the different Al₂O₃ supports used (OMA-Al₂O₃ and SIG-Al₂O₃). In the case of the NiO-30-OMA catalyst, the utilization of the OMA-Al₂O₃ (340 m² g^{−1}) led to a good dispersion of nickel and therefore to the formation of a great amount of small Ni particles with medium MSI. In contrast, the utilization of the SIG-Al₂O₃ (117 m² g^{−1}) results in a poor nickel dispersion and as a result a considerable amount of big Ni particles with low MSI were formed. Regarding high Ni content catalysts (67 mol.%), different Al₂O₃ supports and preparation methods were used to synthesize them. Comparing NiO-67-SIG and NiO-67-SIG2 catalysts characteristics, it can be concluded that textural properties, MSI and nickel crystal domain sizes were dramatically affected by the preparation method. During NiO-67-SIG synthesis, Ni nitrate was added to the already calcined SIG-Al₂O₃. In contrast, Ni and Al nitrates were calcined together in the synthesis of the NiO-67-SIG2 and as a result better textural properties, lower Ni crystal domain size and greater proportion of Ni species with medium MSI were obtained. The interaction between Ni and Al species is improved when their nitrates are calcined together. NiO-67-OMA catalyst

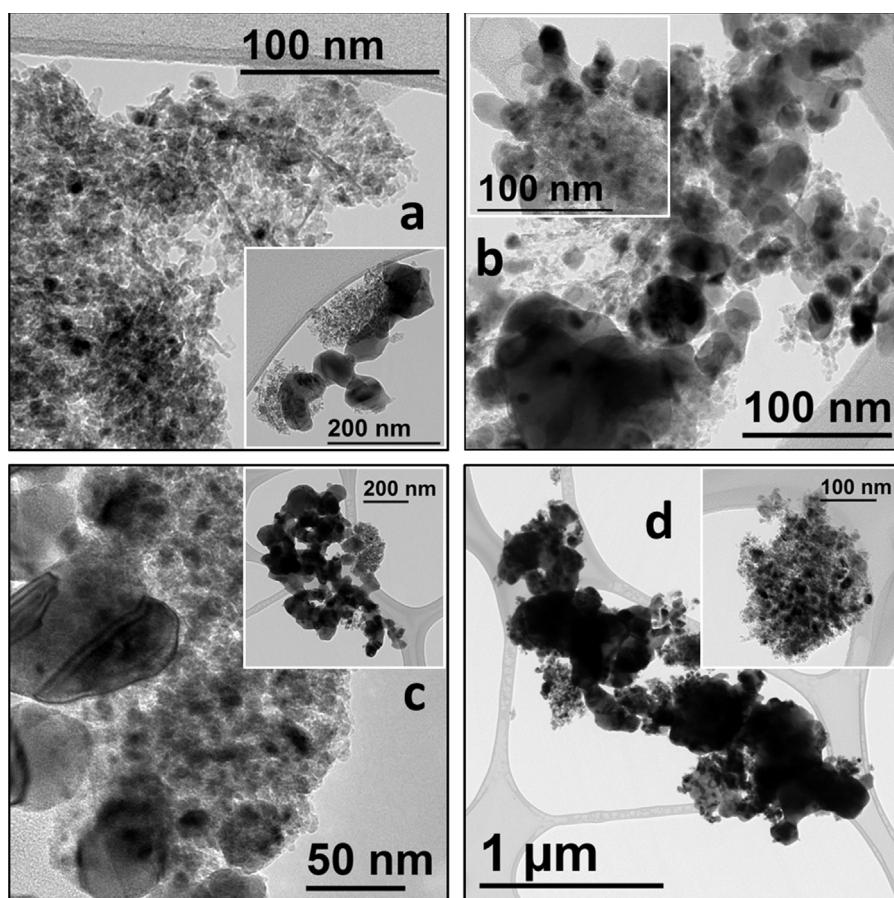


Fig. 2. TEM micrographs of the reduced catalysts. Ni-30-OMA (a), Ni-30-SIG (b), Ni-67-OMA (c) and Ni-67-SIG2 (d).

was prepared using the same method as the one used to prepare the NiO-67-SIG catalyst. However, its characteristics were more similar to those of the NiO-67-SIG2 catalyst. The great S_{BET} , V_p and APD of the OMA- Al_2O_3 counteracted the negative effect of adding the Ni nitrate to the already calcined OMA- Al_2O_3 .

3.2. NCs production and characterization

Catalysts were tested at 700°C , $120\text{ L}_\text{N} \text{ g}_{\text{cat}}^{-1} \text{ h}^{-1}$ and using a $\text{CH}_4:\text{CO}_2$ ratio of 60:40 (v/v) during 180 min to compare its performance in the CDB. Samples recovered after reaction (spent catalyst + deposited carbon) were characterized by different techniques: TEM, XRD, N_2 adsorption and TPO. Carbon yield (expressed per gram of catalyst, $\text{g}_{\text{carbon}} \text{ g}_{\text{cat}}^{-1}$) and nickel, $\text{g}_{\text{carbon}} \text{ g}_{\text{Ni}}^{-1}$, inter-layer spacing (d_{002}), crystal domain size (L_c), Ni crystal domain size (dp_{Ni}) and BET surface area (S_{BET}) of the carbonaceous samples are reported in Table 3.

TEM micrographs of the carbonaceous samples are shown in Fig. 4. Low magnification TEM images of the carbonaceous samples obtained with the Ni-30-OMA, Ni-30-SIG and Ni-67-SIG2 spent catalysts (Fig. 4a, c and e, respectively) revealed the presence of two types of carbon: nanofilamentous carbon (NC) and encapsulating carbon. In all samples both types were observed, although their relative concentrations varied. With the Ni-30-OMA catalysts, carbon was preferentially deposited as NC as suggested by the great amount of this kind of carbon structures in Fig. 4a. At the same time, dark agglomerates were also observed. These agglomerates (Fig. 4b) were composed by carbon (53.2 wt.%), aluminium (33.6 wt.%) and nickel (13.2 wt.%), as revealed the EDX analysis (Fig. S8). Nevertheless, the great carbon percentage is mostly ascribed

to the NCs present in the region analysed. Disregarding carbon contribution, Ni:Al molar ratio was 15:85, far away from the nominal 30:70. This suggests that Ni particles may be lifted off from the Al_2O_3 structure when the NC growing process started. Moreover, the absence of NCs with Ni particles anchored to the Al_2O_3 support suggested a tip growth mechanism [47]. In the case of the Ni-30-SIG catalyst, the concentration of NCs was dramatically reduced (Fig. 4c) and big Ni particles (50–100 nm) encapsulated by graphitic carbon were observed (Fig. 4d). TEM micrographs of the Ni-67-SIG2 spent catalyst revealed an intermediate situation as compared with the previous ones. As it occurred with the Ni-30-SIG spent catalyst, a mixture of NCs and big and encapsulated Ni particles was observed (Fig. 4e and f). However, the concentration of NCs as respect to big Ni particles was much higher in this case. High magnification TEM images were taken in order to analyse which kind of NCs structures were formed and to measure their diameters. In all cases, a mixture of two different types of hollow carbon nanofibers (CNFs) was observed: fishbone (Fig. 4g) and parallel-like (Fig. 4h). Nevertheless, the average size of the NCs varied between samples. Those NCs produced with the Ni-30-OMA and Ni-30-SIG catalysts presented diameters between 10 nm and 25 nm, with an average size of 18 ± 5 nm. In turn, NCs formed with the Ni-67-OMA and Ni-67-SIG2 catalysts were slightly bigger having an average diameter of 29 ± 7 nm. TEM micrographs of the Ni-67-OMA spent catalyst were not shown since same NCs characteristics and structures as those of the NCs obtained with the Ni-67-SIG2 catalyst were observed. In turn, Ni-67-SIG spent catalysts was not characterized by TEM due to the low carbon production obtained (Table 3).

Carbonaceous samples were also characterized by XRD. The presence of an intense peak at ca. 26° revealed a graphitic structure

Table 3
Carbon yield (Y_C), interplanar distance (d_{002}), crystal domain size (L_c), Ni crystal domain size after reaction (dp_{Ni}) and BET surface area (S_{BET}) of the carbonaceous materials obtained after reaction (spent catalyst + deposited carbon).

Catalyst	Y_C		d_{002}	L_c	dp_{Ni}	S_{BET}
	($g_{carbon} g_{cat}^{-1}$)	($g_{carbon} g_{Ni}^{-1}$)				
Ni-30-OMA	4.10	13.52	0.3411	5.2	12.9	116.5
Ni-30-SIG	1.39	4.60	0.3365	11.0	40.5	63.0
Ni-67-OMA	3.92	6.67	0.3360	6.9	29.3	90.6
Ni-67-SIG	0.58	0.98	0.3358	17.4	60.6	n.a.
Ni-67-SIG2	6.29	10.70	0.3381	6.2	28.4	95.5

n.a.: not analysed.

(Fig. S9). According to Franklin's classification [48], the d_{002} values obtained (Table 3) correspond to a turbostratic carbon structures. Turbostratic carbon is generally regarded as a variant of hexagonal high ordered graphite where graphite crystallites have a random orientation and therefore $d_{002,turbostratic} > d_{002,graphite}$. High d_{002} values are associated with highly disordered turbostratic carbons while low d_{002} values are associated with the formation of uniform coatings encapsulating Ni particles [37]. This assumption agrees with our results. The carbonaceous sample obtained with the Ni-30-OMA catalyst presented the highest d_{002} value (0.3411 nm) and as it was observed in Fig. 4a, carbon was mostly deposited as NCs. In contrast, lower d_{002} values (Table 3) were calculated for the other samples, suggesting a greater proportion of encapsulating carbon as observed in Fig. 4c and e. More evident was the trend observed on L_c values (Table 3). The higher the proportion of NCs as respect to encapsulated Ni particles, the lower the L_c value obtained. Probably, carbon crystallites present in the layers encapsulating Ni particles

(Fig. 4d) were larger than those present in the NCs layers (Fig. 4g and h).

No NiO peaks were observed in the XRD patterns of the carbonaceous samples (Fig. S9), indicating that Ni was still in the reduced phase after reaction. Ni crystal domain sizes calculated after reaction are included in Table 3. Average Ni crystal sizes ranged between 12.9 nm (Ni-30-OMA) and 60.6 nm (Ni-67-SIG). It has been extensively reported that metal particles are reformed during the initial period of the reaction in the catalytic decomposition of methane [28,49,50]. Ermakova et al. [51] prepared catalysts with different average Ni crystal sizes ranging from 15 nm to 60 nm before reaction. During reaction, they observed three different behaviours. Small crystals were rapidly regrouped forming crystals of 30 nm and big crystals (~ 60 nm) were both segregated into sizes of 30 nm or remained invariable, depending on the catalyst. In our case, even though a different reaction took place, an increase of the Ni crystal size was appreciated for almost all the catalysts after reaction pointing out that a sintering process took place. Ni crystal size of the Ni-30-OMA, Ni-30-SIG, Ni-67-OMA and Ni-67-SIG2 catalysts changed from 4.0 nm, 32.6 nm, 20.4 nm and 10.9 nm to 12.9 nm, 40.5 nm, 29.3 nm and 28.4 nm, respectively. High reaction temperature (700 °C) and the low MSI of the big Ni particles may be responsible of this situation. In turn, Ni crystal size of the Ni-67-SIG catalyst remained almost invariable, from 58.0 to 60.6 nm. It is noteworthy, that Ni crystal domain size measured after reaction of the Ni-67-OMA and Ni-67-SIG2 catalysts agrees with the diameter of the NCs formed.

Some differences were observed according to S_{BET} values. Samples obtained with the Ni-30-OMA, Ni-67-OMA or Ni-67-SIG2 catalysts, presented surface areas around $100 m^2 g^{-1}$ while the sample obtained with the Ni-30-SIG catalyst presented only a surface area of $63.0 m^2 g^{-1}$. The former catalysts led to a high carbon yield (Table 3) and as a result, the surface area of the samples can be attributed to the deposited carbon. However, the carbon yield obtained with the Ni-30-SIG catalyst was low and the surface area was importantly influenced by the catalyst present in the sample.

Carbon yield (Y_C) was calculated per gram of catalyst ($g_{carbon} g_{cat}^{-1}$) and per gram of Ni ($g_{carbon} g_{Ni}^{-1}$). The production of carbon per gram of catalyst follows this order: Ni-67-SIG2 > Ni-30-OMA > Ni-67-OMA > Ni-30-SIG > Ni-67-SIG (Table 3). It is noteworthy that albeit the Ni:Al molar ratio of the Ni-30-OMA catalyst was much lower than in the Ni-67-OMA catalyst, a slightly higher carbon yield was obtained (4.10 vs $3.92 g_{carbon} g_{cat}^{-1}$, respectively). Besides, when Y_C is expressed per gram of Ni, the Y_C obtained with the Ni-30-OMA catalyst was higher than the one obtained with the Ni-67-SIG2 catalyst (13.52 vs $10.70 g_{carbon} g_{Ni}^{-1}$). Y_C differences between catalysts with the same Ni content were noticed. First, the Y_C obtained with the Ni-30-OMA catalyst was almost three times higher than the one obtained with the Ni-30-SIG catalyst. In turn, Y_C obtained with the Ni-67-SIG2 was 1.6 and 10.8 times higher than the ones obtained with the Ni-67-OMA and Ni-67-SIG catalysts, respectively. The different carbon yields obtained may be related to the different characteristics of the catalysts (Section 3.1), especially with the amount of difficult to reduce

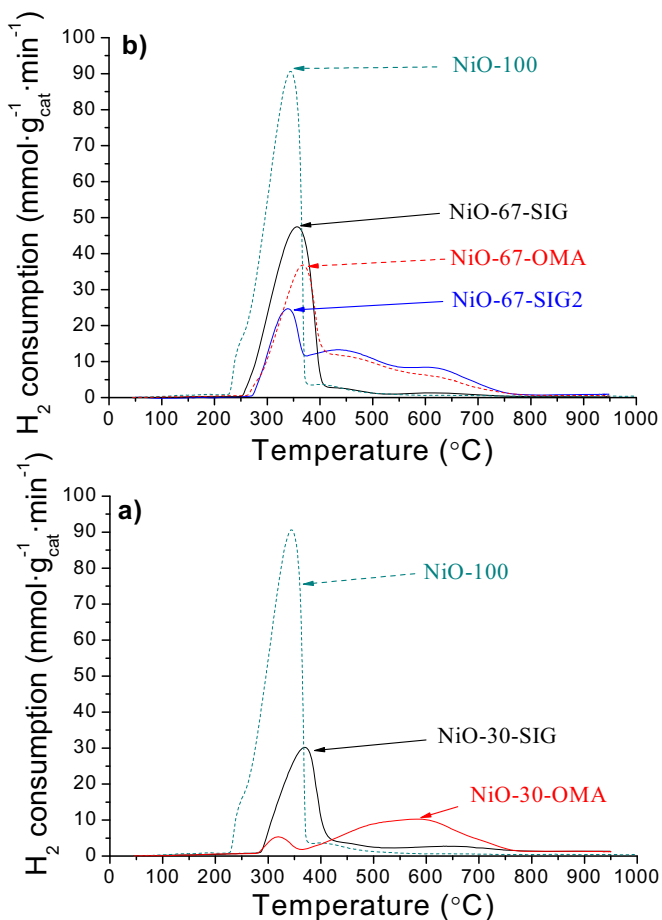


Fig. 3. TPR profiles of calcined catalysts. High Ni content catalysts (a) and low Ni content catalysts (b).

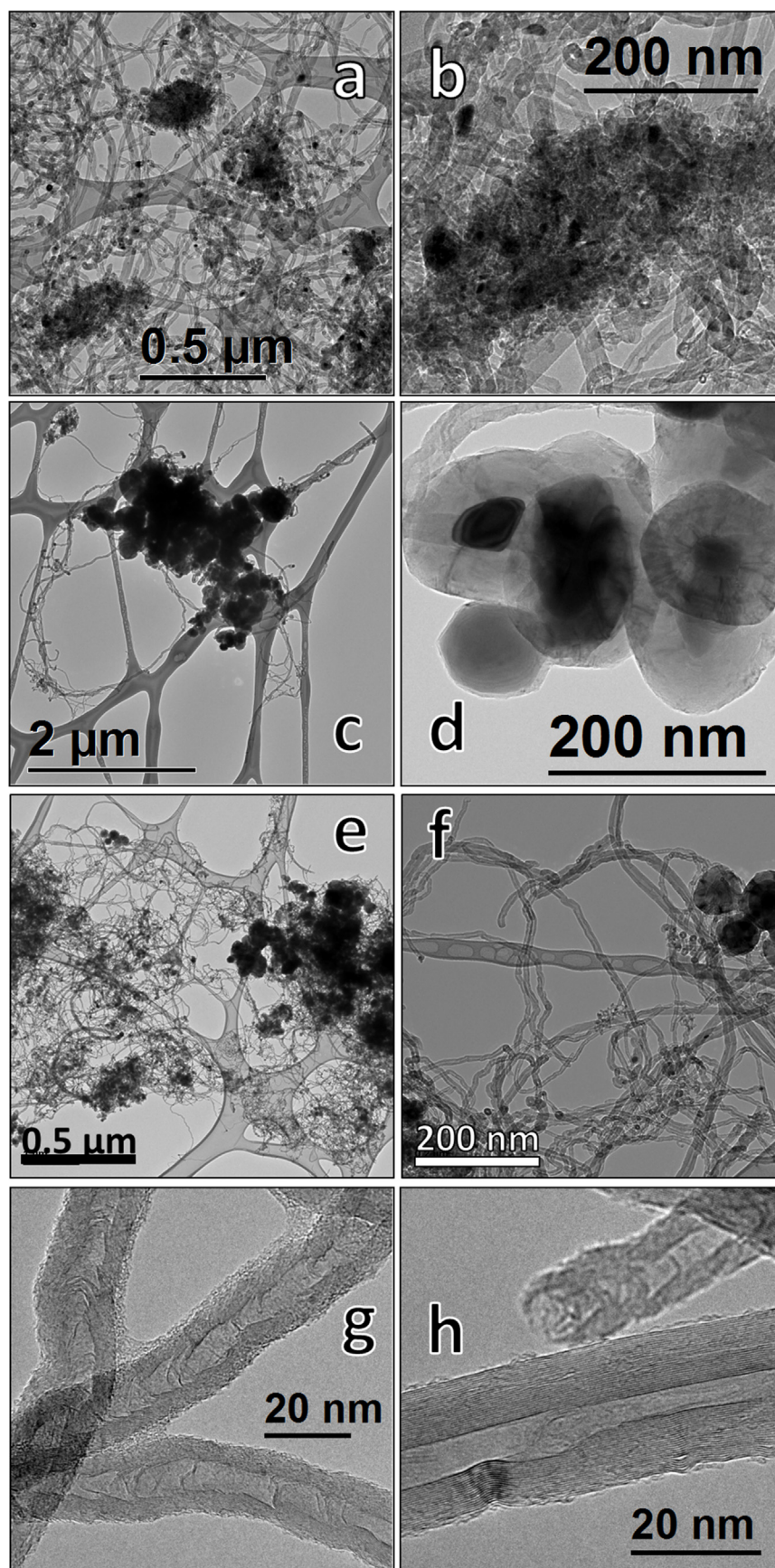


Fig. 4. TEM micrographs of the samples recovered after reaction (carbon + spent catalysts): Ni-30-OMA (a and b), Ni-30-SIG (c and d) and Ni-67-SIG2 (e and f). Micrographs g and h correspond to the samples Ni-30-SIG and Ni-30-OMA, respectively, and are used as an example to show the carbon structures obtained in all cases.

Table 4Syngas composition (v:v, dry basis), CH₄ conversions and CH₄ sustainability factors (S.F._{CH₄}) obtained with the different catalysts after 5 min and 180 min TOS.

Catalyst	TOS (min)	H ₂ (%)	CO (%)	CH ₄ (%)	CO ₂ (%)	X _{CH₄} (%)	S.F. _{CH₄} (–)
Ni-30-OMA	5	38	38	19	6	52	0.70
	180	29	33	28	11	36	
Ni-30-SIG	5	37	35	20	7	48	0.58
	180	26	29	32	14	28	
Ni-67-OMA	5	46	39	12	4	68	0.51
	180	28	31	29	12	35	
Ni-67-SIG	5	28	30	29	13	34	0.69
	180	21	24	37	18	24	
Ni-67-SIG2	5	42	36	16	6	61	0.53
	180	25	29	32	14	32	

Ni species. The higher the amount of these species was, the higher the carbon yield obtained. TPR profiles of the Ni-67-SIG and Ni-30-SIG revealed an absence or a little amount of difficult to reduce Ni species (Fig. 3) and in agreement with the previous assumption, the amount of carbon accumulated was negligible as compared with the one accumulated with the other catalysts. In contrast, Ni-30-OMA, Ni-67-OMA and Ni-67-SIG2 presented a great amount of these species and considerable carbon yields were obtained. It seems that these species presented a suitable MSI that favour the formation of NCs. It was reported that both a too low or too high MSI led to the formation of encapsulating carbon [30,42]. In literature, carbon yield has also been associated to Ni crystal domain size. Pinilla et al. [37] found that carbon yield was highly correlated with the Ni domain size measured after reaction, and the highest Y_C were obtained with those catalysts presenting Ni domain sizes around 15 nm. In turn, Ermakova et al. [51] reported high carbon yields with catalysts presenting Ni crystal sizes after reaction around 30 nm while catalysts with crystal sizes around 60 nm did not led to carbon production. Catalysts presenting high carbon yields, i.e. Ni-30-OMA, Ni-67-OMA and Ni-67-SIG2, presented average Ni crystal sizes after reaction of 12.9, 29.3 and 28.4 nm, respectively. In contrast, Ni crystal sizes of the samples obtained with the Ni-30-SIG and Ni-67-SIG catalysts were 40.5 nm and 60.6 nm and low carbon yields were obtained, especially with the Ni-67-SIG which presented the highest Ni crystal size. As commented before, there is a relationship between MSI and the increase/decrease of the Ni crystal domain size during reaction and therefore both catalyst characteristics are connected and affect carbon yield.

3.3. Catalysts activity and stability

Syngas compositions measured after 5 min and 180 min TOS are included in Table 4 along with CH₄ conversions (X_{CH₄}) and sustainability factors (S.F._{CH₄}).

From a catalytic point of view, worst results were obtained with the Ni-67-SIG catalyst. After 5 min TOS, CH₄ conversion and H₂ and CO concentrations were much lower as compared with those obtained with the other catalysts (Table 4). Beside this, carbon yield after three hours TOS was negligible (Table 3). Low surface area (43 m² g^{−1}), low MSI and big Ni crystal size (58.0 nm) of the reduced catalyst, resulted in a lower amount of active sites and thus in a worse catalytic performance than the other catalysts. For all these reasons, Ni-67-SIG was not included in the following comparison between catalysts and was discarded as an interesting catalyst for the CDB.

Comparing the other catalysts, small differences regarding syngas compositions were observed after 5 min TOS, even though two well different Ni:Al molar ratios (30:70 mol.% and 67:33 mol.%) were used to prepare the catalysts. H₂ concentrations obtained with the high Ni content catalysts were slightly

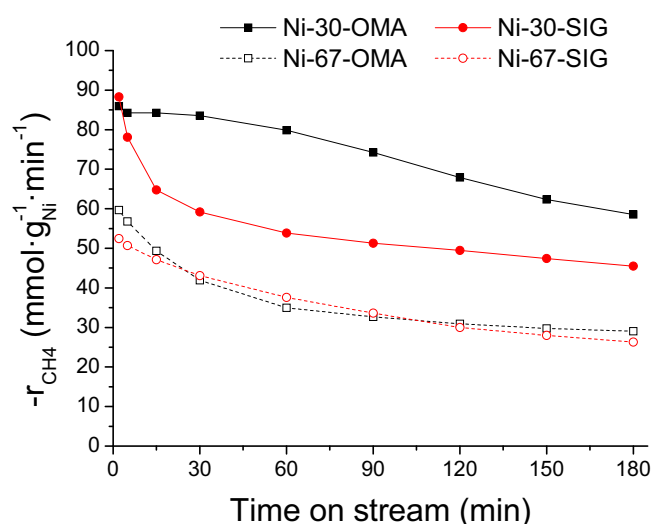


Fig. 5. CH₄ reaction rate ($-r_{CH_4,t}$) as a function of the TOS for the different catalysts, expressed per gram of nickel.

higher than the ones obtained with the low Ni content catalysts while CO concentrations were similar. X_{CH₄,5min} followed this order: Ni-67-OMA > Ni-67-SIG2 > Ni-30-OMA > Ni-30-SIG. Ni-67-OMA and Ni-67-SIG2 catalysts were a little more active than Ni-30-OMA and Ni-30-SIG catalysts, at least at the beginning of the experiment. The higher Ni loading of these catalysts was probably the reason of the behaviour observed. Nevertheless, CH₄ conversion and syngas compositions are not normalized variables and do not take into account the different Ni:Al molar ratios used. For that reason and in order to compare properly the activity of the catalysts, the evolution of $-r_{CH_4}$ over time, expressed per gram of nickel, was plotted in Fig. 5. At the beginning of the experiments, both Ni-30-OMA and Ni-30-SIG presented similar $-r_{CH_4}$ values, higher than those obtained with the Ni-67-OMA and Ni-67-SIG2 catalysts. Furthermore, this situation was maintained throughout the experiment revealing a better performance of the low Ni content catalysts in the process.

In addition, a progressive decrease of $-r_{CH_4}$ with time was observed in all the experiments (Fig. 5). Two different deactivation behaviours were observed. Ni-30-SIG, Ni-67-OMA and Ni-67-SIG2 catalysts presented a sharp decrease of $-r_{CH_4}$ in the first 60 min TOS, especially Ni-30-SIG, and then $-r_{CH_4}$ stabilized. In contrast, $-r_{CH_4}$ evolution of the Ni-30-OMA catalyst remained almost invariable in the first 60 min and then a slow and continuous decrease was observed. In summary, after 180 min TOS, the most stable and active catalyst was the Ni-30-OMA. These two well differentiated

behaviours may correspond to different deactivation mechanisms. According to TEM micrographs (Fig. 2) and TPR profiles (Fig. 3), Ni-30-SIG, Ni-67-OMA and Ni-67-SIG2 catalysts presented an important number of large Ni particles that do not form significant chemical bonds with the Al_2O_3 support. As previously reported [30,37], it may occur that these big Ni particles, active towards CH_4 decomposition at the beginning of the experiment, were deactivated by encapsulating carbon reducing the number of active sites. In the same line, Ermakova et al. [51] suggested that coarse Ni particles were not effective for CH_4 decomposition since the equilibrium between formation of amorphous carbon (CH_4 decomposition), carbon diffusion and NC growth, necessary to maintain the catalyst activity [52], does not take place and as a result catalyst particles are rapidly blocked. In contrast, Ni-30-OMA TEM micrographs (Fig. 2a) and TPR profile (Fig. 3b) did not reveal such amount of these Ni particles and this may be the reason of the stability observed. CH_4 sustainability factors ($\text{S.F.}_{\text{CH}_4}$) of the different experiments were also included in Table 3. Ni-30-OMA catalyst presented the highest stability ($\text{S.F.}_{\text{CH}_4} = 0.70$) followed by the Ni-30-SIG ($\text{S.F.}_{\text{CH}_4} = 0.58$), the Ni-67-SIG2 ($\text{S.F.}_{\text{CH}_4} = 0.53$) and the Ni-67-OMA ($\text{S.F.}_{\text{CH}_4} = 0.51$) catalysts.

4. Conclusions

Excepting Ni-67-SIG catalyst, catalysts showed a good performance and similar results according to syngas compositions were obtained. However, some differences related to stability over time and carbon yields were detected. TPR analysis and TEM micrographs revealed the presence of two different Ni particles. Large Ni particles, with low MSI, favoured the formation of encapsulating carbon and therefore catalyst deactivation. In turn, small Ni particles, presenting a medium MSI, resulted in NCs formation and good catalyst stability. Generally both kinds of Ni particles were observed in all catalysts, however their concentration was dramatically affected by the catalysts synthesis conditions. The use of a high surface area Al_2O_3 (OMA- Al_2O_3) allowed a good dispersion of Ni and as a result small Ni particles were predominantly formed (Ni-30-OMA). Preparation method was also important. The addition of the Ni nitrate to the already calcined Al_2O_3 provoked that almost all the Ni particles were large particles with low MSI (Ni-67-SIG). In contrast, calcining Ni and Al nitrates together resulted in a considerable amount of Ni particles with a medium MSI (Ni-67-SIG2).

Carbon yield, expressed per gram of nickel, obtained with the Ni-30-OMA catalyst was higher than those obtained with the high Ni content catalysts (67 mol.%) and carbon was predominantly deposited as NCs. A mixture of hollow parallel and fishbone like carbon nanofibers were obtained in all cases.

Acknowledgments

The authors acknowledge the Spanish Economy and Competitiveness Ministry and the ERDF funds for the financial support of the Project ENE2011-28318-C03-01. S. de Llobet thanks the Diputación General de Aragón for the Ph.D. grant. Authors would like to acknowledge the use of Servicio General de Apoyo a la Investigación-SAI of the University of Zaragoza.

Appendix A. Supplementary data

Supplementary material related to this article can be found, in the online version, at <http://dx.doi.org/10.1016/j.apcatb.2014.10.014>.

References

- [1] J.L. Walsh, C.C. Ross, M.S. Smith, S.R. Harper, *Biomass* 20 (1989) 277–290.
- [2] E. Ryckebosch, M. Drouillon, H. Vervaeke, *Biomass Bioenergy* 35 (2011) 1633–1645.
- [3] A. Henham, M.K. Makkar, *Energy Convers. Manag.* 39 (1998) 2001–2009.
- [4] S.H. Yoon, C.S. Lee, *Fuel Process. Technol.* 92 (2011) 992–1000.
- [5] A. Domínguez, Y. Fernández, B. Fidalgo, J.J. Pis, J.A. Menéndez, *Energy Fuels* 21 (2007) 2066–2071.
- [6] R. Navarro, B. Pawelec, M.C. Alvarez-Galván, R. Guil-Lopez, S. Al-Sayari, J.L.G. Fierro, *Green Energy Technol.* 137 (2013) 45–66.
- [7] J. Xu, W. Zhou, Z. Li, J. Wang, J. Ma, *Int. J. Hydrogen Energy* 34 (2009) 6646–6654.
- [8] K.-H. Lin, H.-F. Chang, A.C.C. Chang, *Int. J. Hydrogen Energy* 37 (2012) 15696–15703.
- [9] G. Bonura, C. Cannilla, F. Frusteri, *Appl. Catal. B* 121–122 (2012) 135–147.
- [10] H. Er-rbib, C. Bouallou, F. Werckoff, *Energy Proc.* 29 (2012) 156–165.
- [11] E. Finocchio, T. Montanari, G. Garuti, C. Pistorino, F. Federici, M. Cugino, G. Busca, *Energy Fuels* 23 (2009) 4156–4159.
- [12] A. Cabrera-Codony, M.A. Montes-Morán, M. Sánchez-Polo, M.J. Martín, R. Gonzalez-Olmos, *Biogas Upgrading, Environ. Sci. Technol.* 48 (2014) 7187–7195.
- [13] M.P. Kohn, M.J. Castaldi, R.J. Farrauto, *Appl. Catal. B* 144 (2014) 353–361.
- [14] E. Ruckenstein, H.Y. Wang, *Carbon Deposition, J. Catal.* 205 (2002) 289–293.
- [15] S. Corthals, J. Van Nederkassel, H. De Winne, J. Geboers, P. Jacobs, B. Sels, *Appl. Catal. B* 105 (2011) 263–275.
- [16] D.L. Trimm, *Catal. Today* 37 (1997) 233–238.
- [17] J. Guo, H. Lou, L. Mo, X. Zheng, *J. Mol. Catal. A: Chem.* 316 (2010) 1–7.
- [18] C.H. Bartholomew, *Catal. Rev.* 24 (1982) 67–112.
- [19] C. Wang, N. Sun, N. Zhao, W. Wei, J. Zhang, T. Zhao, Y. Sun, C. Sun, H. Liu, C.E. Snape, *ChemCatChem* 6 (2014) 640–648.
- [20] P. Djinić, I.G. Osojnik Črnivec, B. Erjavec, A. Pintar, *Appl. Catal. B* 125 (2012) 259–270.
- [21] J.L. Pinilla, R. Moliner, I. Suelves, M.J. Lázaro, Y. Echegoyen, J.M. Palacios, *Int. J. Hydrogen Energy* 32 (2007) 4821–4829.
- [22] N.M. Rodríguez, J. Mater. Res. 8 (1993) 3233–3250.
- [23] K.P. De Jong, J.W. Geus, *Catal. Rev.* 42 (2000) 481–510.
- [24] P. Serp, M. Corrias, P. Kalck, *Appl. Catal. A* 253 (2003) 337–358.
- [25] S. de Llobet, J.L. Pinilla, R. Moliner, I. Suelves, J. Arroyo, F. Moreno, M. Muñoz, C. Monné, I. Cameán, A. Ramos, N. Cuesta, A.B. García, *Int. J. Hydrogen Energy* 38 (2013) 15084–15091.
- [26] J.L. Pinilla, S. de Llobet, I. Suelves, R. Utrilla, M.J. Lázaro, R. Moliner, *Fuel* 90 (2011) 2245–2253.
- [27] S. de Llobet, J.L. Pinilla, M.J. Lázaro, R. Moliner, I. Suelves, *Int. J. Hydrogen Energy* 37 (2012) 7067–7076.
- [28] S. Helveg, C. López-Cartes, J. Sehested, P.L. Hansen, B.S. Clausen, J.R. Rostrup-Nielsen, F. Abild-Pedersen, J.K. Nørskov, *Nature* 427 (2004) 426–429.
- [29] S. Takenaka, M. Serizawa, K. Otsuka, *J. Catal.* 222 (2004) 520–531.
- [30] Y. Li, D. Li, G. Wang, *Catal. Today* 162 (2011) 1–48.
- [31] H.F. Abbas, W.M.A. Wan Daud, *Int. J. Hydrogen Energy* 35 (2010) 1160–1190.
- [32] M.A. Ermakova, D.Y. Ermakov, G.G. Kuvshinov, L.M. Plyasova, *J. Catal.* 187 (1999) 77–84.
- [33] Y. Li, J. Chen, L. Chang, *Appl. Catal. A* 163 (1997) 45–57.
- [34] S. Takenaka, S. Kobayashi, H. Ogiwara, K. Otsuka, *J. Catal.* 217 (2003) 79–87.
- [35] M.L. Toebes, J.H. Bitter, A.J. van Dillen, K.P. de Jong, *Catal. Today* 76 (2002) 33–42.
- [36] D. Chen, K.O. Christensen, E. Ochoa-Fernández, Z. Yu, B. Tødtal, N. Latorre, A. Monzón, A. Holmen, *J. Catal.* 229 (2005) 82–96.
- [37] J.L. Pinilla, I. Suelves, M.J. Lázaro, R. Moliner, J.M. Palacios, *Appl. Catal. A* 363 (2009) 199–207.
- [38] S. de Llobet, J.L. Pinilla, R. Moliner, I. Suelves, *Fuel* 139 (2015) 71–78.
- [39] S. Corthals, J. Van Noyen, J. Geboers, T. Vosch, D. Liang, X. Ke, J. Hofkens, G. Van Tendeloo, P. Jacobs, B. Sels, *Carbon* 50 (2012) 372–384.
- [40] S. de Llobet, H. Purón, J.L. Pinilla, R. Moliner, M. Millán, I. Suelves, *Microporous Mesoporous Mater.* 179 (2013) 69–77.
- [41] I. Suelves, M.J. Lázaro, R. Moliner, Y. Echegoyen, J.M. Palacios, *Catal. Today* 116 (2006) 271–280.
- [42] C. Li, Y.-W. Chen, *Thermochim. Acta* 256 (1995) 457–465.
- [43] M. Wu, D.M. Hercules, *J. Phys. Chem.* 83 (1979) 2003–2008.
- [44] B. Scheffer, P. Molhoek, J.A. Moulijn, *Appl. Catal.* 46 (1989) 11–30.
- [45] J.L. Pinilla, P. Arcelus-Arillaga, H. Puro, M. Millan, *Appl. Catal. A* 459 (2013) 17–25.
- [46] T. Klimova, M. Calderón, J. Ramírez, *Appl. Catal. A* 240 (2003) 29–40.
- [47] E. Lamouroux, P. Serp, P. Kalck, *Catal. Rev.* 49 (2007) 341–405.
- [48] R. Franklin, *Acta Crystallogr.* 4 (1951) 253–261.
- [49] R.T.K. Baker, M.A. Barber, P.S. Harris, F.S. Feates, R.J. Waite, *J. Catal.* 26 (1972) 51–62.
- [50] Y. Li, J. Chen, Y. Ma, J. Zhao, Y. Qin, L. Chang, *Chem. Commun. (Cambridge, U. K.)* (1999) 1141–1142.
- [51] M.A. Ermakova, D.Y. Ermakov, L.M. Plyasova, G.G. Kuvshinov, *Catal. Lett.* 62 (1999) 93–97.
- [52] S. De Llobet, J.L. Pinilla, M.J. Lázaro, R. Moliner, I. Suelves, *Fuel* 111 (2013) 778–783.